# THESIS FOR THE DEGREE OF LICENTIATE OF ENGINEERING IN THERMO AND FLUID DYNAMICS

Experimental Investigation of ultra-high fuel injection pressure spray for GDI engines

AKICHIKA YAMAGUCHI

Department of Mechanics and Maritime Sciences Combustion and Propulsion Systems CHALMERS UNIVERSITY OF TECHNOLOGY

Gothenburg, Sweden 2020

Experimental Investigation of ultra-high fuel injection pressure spray for GDI engines AKICHIKA YAMAGUCHI

© AKICHIKA YAMAGUCHI, 2020

Thesis for the degree of Licentiate of Engineering 2020:16 Department of Mechanics and Maritime Sciences Combustion and Propulsion Systems Chalmers University of Technology SE-412 96 Gothenburg Sweden Telephone: +46 (0)31-772 5041

Chalmers Reproservice Gothenburg, Sweden 2020 Experimental Investigation of ultra-high fuel injection pressure spray for GDI engines Thesis for the degree of Licentiate of Engineering in Thermo and Fluid Dynamics AKICHIKA YAMAGUCHI Department of Mechanics and Maritime Sciences Combustion and Propulsion Systems Chalmers University of Technology

#### Abstract

Gasoline Direct Injection Engines (GDI) for passenger cars currently use fuel injection systems operating at pressures of up to 350 bar. Injection pressures have increased over time, and there is evidence that particulate emissions could be reduced by raising them further, up to 500 bar. However, it is not clear whether further beneficial effects would be achieved by using higher injection pressures exceeding 600 bar. This thesis presents experimental studies on sprays and combustion conducted to assess the benefits and downsides of substantially increased fuel injection system pressures (between 200 and 1500 bar) in GDI engines. Experiments on spray characteristics and spray-air interaction revealed that raising the injection pressure from 200 to 600 bar significantly improved spray atomization. This pressure effect on atomization became less significant when the injection pressure was over 800 bar. High pressure sprays also evolved much faster than low pressure ones, but the spray tip penetration at the end of injection did not vary greatly with the injection pressure. High pressure sprays induced more air flow because of their high velocity and good atomization, which increased the likelihood and strength of spray-air interactions. These results indicate that high injection pressures result in better mixture formation because they accelerate evaporation and induce stronger air flow. However, spray impingement caused by high spray velocities and penetration may cause problems during engine operation.

Keywords: GDI engine, Spray, High Pressure, Spray imaging, Spray tip penetration, PDI, drolet size, PIV, Air entrainment

### LIST OF PUBLICATIONS

This thesis is based on the work contained in the following publications:

- Publication A A. Yamaguchi, L. Koopmans, A. Helmantel, F. P. Karrholm and P. Dahlander, "Spray Characterization of Gasoline Direct Injection Sprays Under Fuel Injection Pressure up to 150 MPa with Different Nozzle Geometries" in SAE Technical Paper 2019-01-0063.
- Publication B A. Yamaguchi, L. Koopmans, A. Helmantel, J. Dillner and P. Dahlander, "Spray-induced air motion by ultra-high injection pressure sprays for gasoline direct injection engines" under review in SAE International Journal of Fuels and Lubricants.

### Acknowledgements

Throughout the writing of this licentiate thesis I have received a lot of support and assistance.

I would first like to thank my supervisor, Prof. Petter Dahlander. We have discussed project direction and experiment quite often, and these discussions always helped me to carry on my project in the right direction.

I would like acknowledge the project members, Lucien Koopmans, Ayolt Helmantel, Johan Dillner, Michael Oevermann and Sandip Wadekar. You often gave me critical feedbacks and advices in the project meetings. I should mention that I got a lot of hardware support from Volvo Cars and DENSO Sweden. It is impossible to conduct unique tests without unique hardwares and technical supports from both companies.

I would also like to thank seniors and colleagues for making great atmosphere in our division. Good time in this division always made me fresh and motivated me to work more.

# Contents

$\mathbf{A}$	stract	i
$\mathbf{Li}$	t of publications	iii
A	knowledgements	v
1	Introduction	1
<b>2</b>	Background	9
	2.1 Spray characteristics for GDI engines	. 9
	2.1.1 Injector type and spray shape	. 9
	2.1.2 Atomization	. 11
	2.1.3 Spray Penetration	. 13
	2.1.4 Droplet Size Distribution	. 14
3	Experimental setup	17
	3.1 Injector	. 17
	3.2 Fuel pump	. 18
	3.3 Injection rate meter	. 19
	3.4 Spray Imaging	. 21
	3.5 Phase Doppler Interferometry	. 22
	3.6 Particle Image Velocimetry	. 23
<b>4</b>	Methodology	27
	4.1 Spray image	
	4.2 Droplet size	. 27
	4.3 Large-scale air motion	. 29
<b>5</b>	Summary of Results	31
	5.1 The effect of ultrahigh injection pressures	. 31
	5.2 The effect of the nozzle type	. 34
6	Future work	39
	6.1 Studies on mixture formation in an optical engine	. 39
	6.2 Single-cylinder engine tests with an improved injector	. 39

References

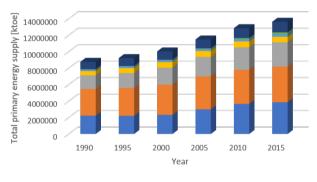
# I Appended Papers A–B

41

 $\mathbf{45}$ 

# 1 Introduction

Technological development has enhanced human quality of life and changed our lifestyles dramatically. However, while it is hard to imagine life without modern technologies such as electricity, phones, and transportation, our heavy use of these technologies has caused global power consumption to increase steadily over time (see Figure 1.1) [1]. Partly as a result, we are facing a range of environmental problems including climate change, depletion of natural resources, and pollution that are at least partly due to our ever-growing energy consumption.



■ Coal ■ Oil ■ Natural gas ■ Nuclear ■ Hydro ■ Wind, solar, etc. ■ Biofuels and waste

Figure 1.1: Total primary energy supply by source, World 1990-2015 [1].

Many of the transportation technologies that we use on a daily basis rely on the combustion of fossil fuels. This has a significant environmental impact, contributing to climate change and oil depletion. Overall, the transportation sector accounts for around 30 % of the world's total energy consumption, as shown in Figure 1.2 [2]. Consequently, there is an urgent need to reduce its environmental impact. The automotive industry has sought to address this need by introducing new systems such as hybrid engines and common-rail systems for diesel systems. Governments have spurred this process by introducing strict regulations such as the EU's EURO 6d Temp regulations of 2017 (see Table 1.1) [3]. This process will continue; more stringent standards will come into force in the coming years (see Figure 1.3) [4]. These standards typically impose limits on  $CO_2$  and particulate emissions, the reduction of which is a major challenge for both governments and the automotive industry.

There is great interest electrification of cars among automotive manufacturers because such vehicles produce zero tail-pipe emissions. However, the usefulness of full electric vehicles continues to be limited by factors such as low cruise distances and long charging times. To overcome these challenges, hybrid vehicles with both battery electric systems and conventional internal combustion engines (ICE) are increasingly being used. The two

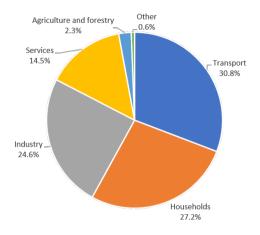


Figure 1.2: Energy consumption by sector across the EU-28 in 2017 [2]

Table 1.1:	Emission	$\operatorname{standards}$	introduced	after	Euro	4	for	gasoline-fueled	passenger
vehicles [3].									

Stage	Date	Cycle	CO	THC	NMHC	NOx	$_{\rm PM}$	PN $[\#/km]$
Euro 5	2009	NEDC	1.0	0.10	0.068	0.060	0.005	-
Euro 6b	2014	NEDC	1.0	0.10	0.068	0.060	0.005	$6.0 \times 10^{11}$
Euro 6d Temp	2017	WLTC (RDE)	1.0	0.10	0.068	0.060	0.005	$6.0 \times 10^{11} \ (9.0 \times 10^{11})$
Euro 6d	2020	WLTC (RDE)	1.0	0.10	0.068	0.060	0.005	$6.0 \times 10^{11} (9.0 \times 10^{11})$

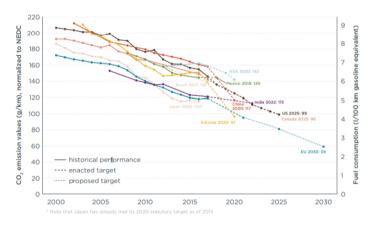


Figure 1.3: Past and future  $CO_2$  emission standards [4].

power sources in these vehicles are used to complement one-another and increase overall efficiency. A recent BCG report predicts that the number of hybrid vehicles will increase markedly in the near future (see Figure 1.4 [5]): by 2030, almost half of all newly sold vehicles are expected to be either hybrid or full electric vehicles. However, non-hybrid

vehicles with only ICE will remain abundant, and over 80 % of operational cars will have an ICE. Therefore, the ICE will play a major role in future propulsion systems, and new ICE designs with improved fuel efficiency and emissions profiles are needed to reduce adverse environmental impacts.

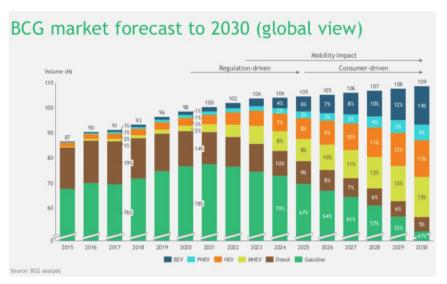


Figure 1.4: Automotive market forecasts [5]

There are two common types of ICE that use different fuel types: gasoline and diesel engines. Gasoline engines are used mainly in passenger cars whereas diesel engines are used in both light and heavy duty vehicles. Gasoline engines use two different fuel injection strategies: Gasoline Direct Injection (GDI) and Port Fuel Injection (PFI). GDI has become increasingly popular in recent years because it offers greater fuel efficiency than PFI [6]. Fuel is injected directly into the cylinder in GDI engines whereas in PFI engines it is injected into the intake manifold. In GDI engines, the fuel is typically injected during the intake stroke to prepare a well-mixed homogeneous mixture before ignition, so combustion proceeds under homogeneous conditions. The time available for fuel-air mixture formation in GDI engines is much shorter than in PFI engines, so GDI engines use relatively high fuel injection pressures (around 250-350 bar in modern examples) to ensure that the injection process is completed quickly [7]. The major benefits of GDI relative to PFI are:

- Lower fuel consumption due to lower pumping losses, higher compression ratios, lower octane requirements, and increased volumetric efficiency
- More precise air-fuel ratio control
- No manifold fuel film formation
- Clean cold-start behavior

GDI engines also have drawbacks relative to their PFI counterparts, namely:

- Increased particulate emissions
- Reliance on complex control and injection technologies
- Higher system costs due to high pressure fuel components
- Fuel pump losses
- Increased electrical power and voltage requirements to drive injectors and pumps

Particulate emissions are a particularly important challenge for GDI engines due to increasingly stringent regulations such as EURO 6d [3]. Finding ways to eliminate these drawbacks without sacrificing any of the advantages mentioned above is a key goal in GDI engine research and development. One promising approach is to simply increase the fuel injection pressure; accordingly, injection pressures in production GDI engines have risen steadily over time. The first production GDI engines used fuel injection pressures around 100 bar, but 200 bar systems are now commonplace. More recently, some companies have started introducing systems with much higher injection pressures of up to 350 bar [8,9]. Moreover, researchers have examined the effects of using injection pressures of 600 bar and above [10–21]. The key outcomes of these studies were:

- Higher injection pressures increase spray velocity, leading to longer spray penetration at any given timing after SOI.
- Higher injection pressures lead to smaller droplet sizes; significant changes in droplet size occur in the relatively low pressure range of 200 bar to 400 bar.
- Particulate emissions are reduced by increasing the injection pressure but the magnitude of the reduction is highly sensitive to injection timings because of piston/wall wetting.

While the above findings are important and valuable, there remain issues that warrant further investigation. For example, while a number of studies have examined injection pressures of up to around 600 bar, few have examined pressures above 1000 bar. Moreover, most studies that have examined such high injection pressures focused on sprays emitted from single hole diesel injectors or applied only a limited range of test conditions. Additionally, many studies on the effects of high injection pressures have used a fixed injection duration, meaning that the injection mass is varied at the same time as the injection pressure. Constant injection durations are very rarely used in metal engine tests because specific operating points require a specific injection mass. There is a need for more information on spray behavior when using injection pressures above 1000 bar with a constant injection mass, and for a deeper understanding of the relationship between injection pressure, spray behavior, and combustion outcomes.

Another challenge arising from the use of high injection pressures in GDI engines relates to controlling the spray's behavior and evolution. If spray shape and direction are not properly controlled, extensive wall wetting may occur. Nozzle shape is a key determinant of spray shape and properties, and its effect on spray behavior in GDI engines has been investigated by some authors [22, 23]. While some studies have explored the effects of different nozzle shapes on the properties of sprays formed at high injection pressures in diesel engines, there have been no comparable studies on GDI engines combined with high pressure system.

The results of these studies on ultra-high pressure spravs for GDI engines raise a number of questions. The first relates to the point at which the effect of raising the injection pressure reaches saturation. Higher injection pressures are known to have favorable effects on droplet size and particulate emissions up to at least 600 bar, but it is not yet clear whether further improvements can be achieved by using pressures of 1000 bar or more. If there is a saturation point for the injection pressure, it can be concluded that the injection pressure should be around the saturation point and there would be little value in using ultra-high injection pressures such as 2000 bar. The second question relates to the reasons for the observed reduction in particulate emissions upon increasing the injection pressure. Particulate emissions are normally generated from liquid fuel, in fuel films or mixtures. High pressure sprays exhibit better atomization and induce more turbulence than lower pressure sprays, but it is not clear which of these effects has the greater impact on particulate emissions. While particulate emissions are particularly important because they will be targeted by forthcoming emissions standards, it also remains to be determined how high injection pressures affect emissions of other pollutants (e.g. CO and NOx) and engine performance (measured in terms of, e.g., combustion stability and flame speed). If ultrahigh injection pressures adversely affect other emissions or performance, it may be best to use high pressure systems only under limited conditions or in combination with other technologies such as hybrid powertrains. More knowledge is thus needed to determine how best to utilize high injection pressure systems.

To answer these questions, one needs an experimental system that generates ultra-high injection pressures and controls injections precisely. Such a system was created during the course of the work presented here. This system uses a custom-made high pressure fuel pump to deliver injection pressures between 200 bar and 1500 bar. Consequently, the maximum injection pressure deliverable with the new system greatly exceeds both the highest injection pressure currently used in a production engine (350 bar) and the injection pressures commonly used in engine research (500 - 600 bar). Accurate control of the injection duration is achieved by using a diesel injector. However, normal diesel nozzles are inappropriate for GDI sprays and engines, so the injector was fitted with a modified nozzle designed to produce a spray shape similar to that generated by conventional GDI injectors. Details of this unique system are presented in the setup section.

Using this unique apparatus, this project investigates spray characteristics, spray-air interaction, and spray thermal properties to understand the mechanisms responsible for the behaviors observed at high injection pressures and answer the research questions. Emissions depend on combustion quality, which in turn is highly sensitive to the degree of wall wetting and the efficiency of mixture formation. Wall wetting is caused by spray

impingement on the wall, and the level of wetting that occurs depends on various spray properties (spray tip penetration, spray jet velocity, droplet size, and spray target) as well as the in-cylinder flow and the injection strategy (notably, the start of injection timing and the use of single or multi-injection strategies). Meanwhile, mixture formation depends on the rate of fuel droplet evaporation, the in-cylinder air flow (turbulence), and the spray distribution. Several different physical spray characteristics and processes thus influence wetting and mixture formation, and hence emissions. Consequently, to understand the effects of ultrahigh injection pressures on emissions, it is essential to understand basic physics of the spray, as shown in Figure 1.5.

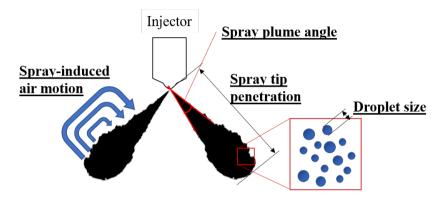


Figure 1.5: Major physics of spray

Quantification is needed to understand spray behavior, as shown in Figure 1.5. The aim of this project was not to develop new measurement systems, so spray characterization was performed using established optical measurement methods. Spray shape characteristics such as spray tip penetration were determined by spray imaging with high speed video cameras. After the start of injection, the camera continuously captured the spray's evolution, enabling time-resolved computation of spray tip penetration. The spray images were also used to calculate spray plume angles. Droplet size was quantified by Phase Doppler Interferometry (PDI), which is an extension of Laser Doppler Velocimetry (LDV). This method is explained in detail in the setup section. Spray-induced air motion was characterized by Particle Image Velocimetry (PIV), which involves seeding small tracer particles into the fluid and monitoring the movement of those particles using a camera. The flow velocity is then calculated from the travel distance of the particles and their delta time.

While there have been some previous studies on high injection pressure sprays and thermal tests using real engines are needed to fully clarify the effects of high injection pressures, spray investigations are needed to understand why these effects occur. To provide a comprehensive understanding of spray formation mechanisms and combustion behavior in GDI engines using ultrahigh injection pressures, the project of which this thesis is a part involved four major campaigns focusing on basic spray characteristics, spray-air interac-

tion, spray behavior inside the cylinder, and thermal profiling. This thesis summarizes the experimental work done within the project on the effects of injection pressure and nozzle shape on basic spray behavior and spray-induced air motion.

# 2 Background

Fuel injection systems for internal combustion engines have undergone extensive development since the time when automobiles used carburetors. Carburetors were largely replaced by Port Fuel Injection (PFI), which remained the system of choice for a long time because it offered a better emissions profile and more accurate control of injection masses. However, PFI offers only limited scope for improving thermal efficiency and varying the injection timing. Gasoline Direct Injection (GDI) subsequently emerged as an attractive alternative for improving engine performance because of its cooling effect and because it enables accurate control of both injection mass and timing. GDI works particularly well when combined with engine downsizing, and there is considerable ongoing research and development activity focused on improving GDI systems. A drawback of GDI is that it produces relatively high particulate emissions because direct injection tends to shortern mixing times and to favor the formation of fuel films on engine components. These high particulate emissions are a significant barrier to compliance with modern emissions standards such as Euro 6d-TEMP (which came into force in 2019) and the more stringent new regulations that will come into force in the near future. Consequently, there is great interest in finding ways to retain the advantages of GDI while reducing particulate emissions.

## 2.1 Spray characteristics for GDI engines

In GDI engines, the characteristics of the fuel spray strongly affect fuel/air mixture formation, which in turn influences combustion behavior. Spray characteristics also affect fuel film formation and turbulence, as shown in Figure 2.1. Efficient operation of GDI engines requires precise control over the mass of injected fuel and for the injected fuel to be atomized as quickly as possible without forming fuel films on engine components. Atomization is the process of breaking large fuel droplets up into smaller ones; smaller droplets evaporate more rapidly, leading to better mixture formation. Film formation depends on spray properties such as the spray direction and spray tip penetration, which must therefore be tightly controlled. Atomization can be improved by increasing the fuel injection pressure, and spray behavior can be adjusted by optimizing the nozzle design.

### 2.1.1 Injector type and spray shape

There are three main type of nozzles for GDI engines: multihole, outward-opening, and swirl nozzles. Figure 2.2 shows the structural differences between these nozzle types and the different spray shapes they produce [24]. The nozzle needle moves inwards in both multihole and swirl nozzles, but these two nozzle types produce rather different spray shapes. Multihole nozzles create multiple spray plumes that develop more or less in alignment with the nozzle hole axis. Conversely, swirl nozzles create hollow cone-shaped sprays because of swirl flow inside the nozzle. Like swirl nozzles, outward-opening nozzles also create hollow cone sprays. However, the shape of these sprays differs from those emitted by swirl nozzles because of differences in the internal nozzle flow and spray

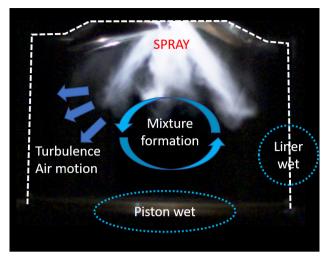


Figure 2.1: Spray behavior in the combustion chamber.

development (see Figure 2.3) [25]. The advantages and drawbacks of these three nozzle types are shown in Figure 2.4 [26]. Swirl nozzles have a number of benefits but these are most pronounced at relatively low injection pressures (around 100 bar). Significantly different outcomes may be observed at higher injection pressures (> 400 bar) because high pressure sprays exhibit improved atomization and greater robustness against fouling.

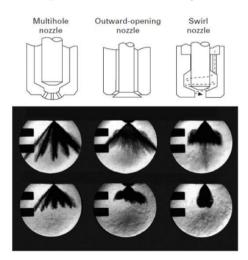


Figure 2.2: Differences between nozzle1shapes and the sprays they produce [24]

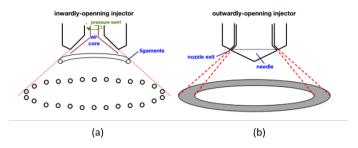


Figure 2.3: Schematic depictions of hollow-cone sprays and film structures. (a) Swirl nozzle. (b) Outward-opening nozzle [25].

Nozzle type	Multihole nozzle	Outward- opening nozzle	Swirl nozzle
Structurew			
Flexibility of spray pattern	++	+	+
Potential for inclined of spray axis	+	-	++
Atomization quality at 100 bar	-	0	++
Robustness against fouling	-	++	+

Figure 2.4: Properties of the three nozzle designs [26].

### 2.1.2 Atomization

The conversion of pressurized fuel into a combustible fuel-air mixture is a key process during fuel injection. Atomization is the process whereby the bulk liquid fuel is converted into small droplets that evaporate readily. It occurs in two stages that are known as primary and secondary break-up (see Figure 2.5) [27]. Primary break-up is dominated by the cavitation in the nozzle flow and results in large ligaments and droplets that form a dense spray near the nozzle. Cavitation is influenced by the injection pressure, nozzle hole geometry, and the properties of the fuel and surrounding medium. Secondary break-up is driven by disruption of consolidating forces, particularly the surface tension of the liquid. Surface tension tends to cause liquid droplets to adopt spherical shapes to minimize their surface area to volume ratio. The surface tension of a liquid is closely related to its viscosity. Aerodynamic forces counteract the consolidating effect of surface tension, leading to droplet break-up.

#### Primary break-up

Primary break-up can occur via several modes, as shown in Figure 2.6. *Rayleigh breakup* is caused by surface tension-induced growth of axisymmetric oscillations of the jet surface.

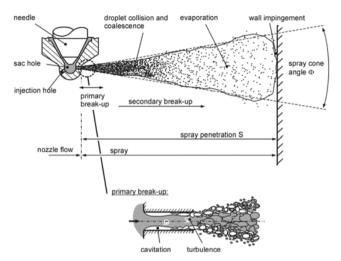


Figure 2.5: Break-up of a full-cone diesel spray [27]

The resulting drop diameters are comparable to the nozzle diameter. First wind-induced breakup is caused by an increase in surface tension due to the relative velocity of the jet and the ambient gas. This creates a static pressure distribution across the jet, accelerating the breakup process. The resulting drop sizes are generally similar to the jet diameter. Second wind-induced breakup is caused by the unstable growth of short-wavelength surface waves on the jet surface. This wave growth is opposed by surface tension. Average drop diameters are smaller than the jet diameter. Finally, in the atomization regime, the jet is disrupted completely at the nozzle exit. Average droplet diameters are thus much smaller than the jet diameter. The relative contributions of these modes depend heavily on three dimensionless parameters: the Weber, Reynolds, and Ohnesorge numbers [28]. The Weber number describes the ratio of the inertial forces to the surface tension, and is defined by equation 2.1; it depends on the relative velocity v, density of the liquid  $\rho_l$ , nozzle hole diameter D, and surface tension  $\sigma$ .

$$We_l = \frac{v^2 D\rho_l}{\sigma} \tag{2.1}$$

The Reynolds number describes the relationship between the internal forces and the viscous force of fluid flow, and is computed using equation 2.2. The contributions of the internal forces depend on the liquid velocity v, the density of the liquid  $\rho_l$ , and the nozzle hole diameter D, while the contribution of the viscous forces depends on the dynamic viscosity of the liquid  $\mu_l$ .

$$Re = \frac{vD\rho_l}{\mu_l} \tag{2.2}$$

By eliminating the jet velocity v, Ohnesorge derived the dimensionless Ohnesorge number, which depends on key fluid properties (the dynamic viscosity  $\mu_l$ , the surface tension  $\sigma$ , and the density of the liquid  $\rho_l$ ) and the nozzle hole diameter D [29].

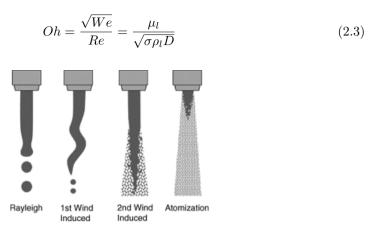


Figure 2.6: Typical breakup regime with a plain-orifice liquid injection nozzle [28]

#### Secondary breakup

Secondary breakup occurs after primary breakup. Its progression depends on the balance between the consolidation force acting on the droplet and the disruption force. The consolidation force acts to preserve the droplet's shape, whereas the disruption force is drag caused by the velocity of the droplet relative to the ambient gas. If the disruption force is stronger than the consolidation force, the droplet breaks up into smaller droplets. The balance between these forces is described by Equation 2.4, where the left-hand term represents the consolidation force and the right-hand term represents the disruption force. D is the droplet diameter,  $\sigma$  is the surface tension,  $U_R$  is the relative velocity between the droplet and the ambient gas, and  $C_D$  is the drag coefficient. Surface tension is main determinant of the consolidation force, and the relative velocity, droplet diameter, and gas density are the main determinants of the disruption force.

$$\pi D\sigma = \frac{1}{2}\rho_a U_R^2 C_D \frac{\pi D^2}{4} \tag{2.4}$$

#### 2.1.3 Spray Penetration

The spray penetration is the length of the liquid-phase spray plume from the nozzle tip (see Figure 2.5). It is the main parameter used to describe spray characteristics and behavior because the spray will impinge on the piston/liner if the penetration is too long. The development of a typical diesel spray is shown in Figure 2.7 [30]. Penetration depends on the relative magnitudes of two opposing forces: (1) the kinetic energy of the initial liquid jet and (2) the aerodynamic resistance of the surrounding gas. The initial jet velocity is usually high, but as atomization proceeds and the surface area of the spray increases, the kinetic energy of the liquid is gradually dissipated by frictional losses to the gas. When the drops have finally exhausted their kinetic energy, their subsequent trajectory is dictated mainly by gravity and/or the movement of the surrounding gas.

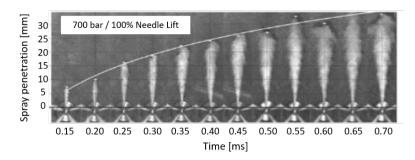


Figure 2.7: Spray dispersion by time [30]

#### 2.1.4 Droplet Size Distribution

The droplet size distribution describes the size of the droplets comprising the spray. A typical size distribution is shown in Figure 2.8 [31]. Size distribution curves are typically either number- or volume-based. Volume-based size distributions are weighted towards larger droplets, so the resulting graphs are right-skewed compared to the corresponding number-based size distributions (see Figure 2.9 [31]). GDI sprays generally have an arithmetic mean diameter of 10 to 20  $\mu$ m, whereas PFI sprays generally have a much larger mean diameter of around 100  $\mu$ m. Increasing the injection pressure improves atomization, reducing the size of the droplets in the spray and shifting the peak of the size distribution curve to the left.

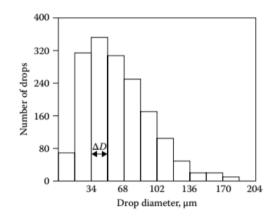


Figure 2.8: A typical droplet size distribution [31].

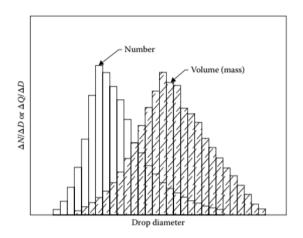


Figure 2.9: Droplet size distributions based on number and volume [31].

# 3 Experimental setup

## 3.1 Injector

The injector is a key component of the fuel injection system that controls the the injection mass and spray behavior at a given injection timing. The injection process is important in GDI engines because spray behavior in cylinder strongly affects engine performance. One of the objectives of this project is to identify injector nozzle shapes that maximize the benefits achieved by using high injection pressures. To this end, experiments were conducted to determine how nozzle shape affects spray characteristics and to gather data to support the development and validation of models to be used in spray simulations. Four different injectors were used in this campaign; their specifications are listed in Table 3.1. Typical injector capable of withstanding pressures of up to 1500 bar was used in the experimental system. A range of modified nozzle types were used with this injector. The injector body is based on a mass-production model manufactured by the DENSO corporation. The tested nozzles have different shapes and numbers of holes, and the ratio of the nozzle thickness to the hole diameter (L/D) was higher than is typical for GDI injectors to enable the nozzles to withstand high injection pressures.

Table $3.1$ :	Injector	specifications
---------------	----------	----------------

	Injector $\#1$	Injector $#2$	Injector $#3$	Injector $#4$
Hole shape	Divergent	Convergent	Divergent	Cylindrical
Number of holes	6	6	10	10
Mass flow rate		15  mg/ms	at $200 \text{ bar}$	
L/D	5.45	5.56	5.34	5.47
Cone angle of hole	15	2	15	0

In this context, a divergent nozzle is one where the inlet diameter is smaller than the outlet diameter; the opposite is true for a convergent nozzle. Schematic depictions of the nozzles' hole configurations and hole arrangements are shown in Figure 3.1 and Figure 3.2. All four injectors were operated at a common flow rate chosen to be representative of the flow rate in a typical GDI injector. This required each nozzle to have a different minimum diameter.

These injectors are driven by piezoelectric actuators, enabling quick and accurate control of needle movement. The opening and closing of the needle is driven by the difference in pressure between the fuel injection and the return flow; the mechanism of the needle's movement is shown in Figure 3.3 [32]. An injection event can be divided into three main stages: non-injection, injection, and after injection. During the non-injection stage, the pressure in the control chamber and in the bottom of the nozzle needle are identical to the injection pressure, so the needle is closed due to the difference in the surface areas. A voltage is applied when the injection starts, causing the piezoelectric actuator to expand. The force from the actuator is transmitted to the control valve through the large and small

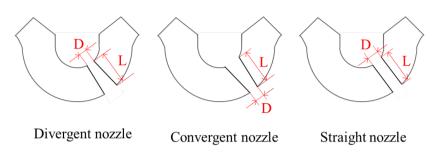


Figure 3.1: Schematic depiction of the nozzle shapes.

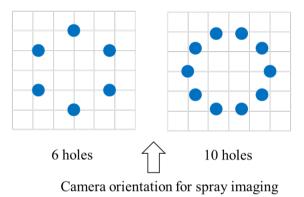


Figure 3.2: Spray targets for 6- and 10-hole injectors.

diameter pistons. This transmitted force causes the control valve to open, at which point fuel is discharged from the control chamber to the return flow side, reducing the pressure in the control chamber. The resulting difference in pressure between the control chamber and the bottom of the needle causes the needle to rise. When the voltage is cut off, the pistons and the control valve in the control chamber rise. This opens the lower seat and closes the upper seat. The pressure in the control chamber then immediately becomes equal to the injection pressure, causing the needle to be pushed down and stopping the injection.

## 3.2 Fuel pump

The model fuel typically used in spray investigations focusing on GDI-type sprays is n-heptane, which has relatively low density and low lubricity. This lubricity is a serious issue for high pressure pumps such as commercial diesel and GDI pumps because it causes plunger seizure. Adding a lubricant improver prevents this but may change the spray's behavior. Furthermore, pulsations from the plunger can create pressure fluctuations, which may also affect spray behavior. To avoid these undesired effects, a custom-made

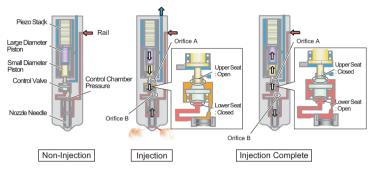


Figure 3.3: Injection mechanism [32]

fuel pump was used in this work to generate fuel pressures up to 1500 bar. This pump consists of a controller, a magnetic valve, a hydraulic oil pump, a low pressure pump, and a main high pressure piston. The hydraulic oil pump drives the main piston, while the low pressure pump feeds the fuel from the fuel tank to the piston. The volume inside the cylinder is around 100 cc. The piston pressurizes fuel to a preset value, and the regulator valve feeds high pressure fuel to the injector. This custom-made pump exhibits high wear resistance and is less prone to pressure pulsations than conventional pumps because the fuel is pressurized by single movement of the piston. This minimizes undesired effects on spray behavior.

### 3.3 Injection rate meter

Injection rates were measured with a Loccioni Nexus 2 Zeuch-type injection rate meter (see Figure 3.4). The main purpose of performing such measurements is to understand the injector's flow characteristics and the relationship between the injection pulse and the actual injected mass. The injection rate meter system consisted of a control chamber, a pressure sensor, a regulation valve, and a Coriolis meter. These components are depicted schematically in Figure 3.5. The control chamber was pre-pressurized with fuel up to a pre-defined back pressure, and the effect of this back pressure on the injection rate was investigated. This feasibility test showed that higher back pressures suppressed noise in the injection rate signal, so the highest possible back pressure (25 bar) was used in this work. There was a continuous outflow due to injections, and the needle of the regulation valve was adjusted automatically to maintain the specified back pressure inside the control chamber. When the injector injected fuel into the pressurized control chamber, the pressure sensor detected the resulting pressure wave. The signal of the pressure wave was then filtered and post-processed to derive the injection rate. The Coriolis meter accurately measured the injection mass and the mean mass flow, which were used to calculate the injection rate. The injectors were mounted in a custom-made injector fixture designed to ensure that the mechanical vibrations of the injector's actuator would have minimal effects on the pressure signal. The system's backpressure was set to a value significantly higher than that expected in a real engine to suppress internal cavitation

in the hydraulic volume. High back pressures generally have only minor effects on the injection rate, and were found to have no significant impact in this work. The injection frequency, injection duration, chamber pressure and signal analysis were controlled by the Loccioni software. The experimental conditions are listed in Table 3.2.



Figure 3.4: Injection rate meter.

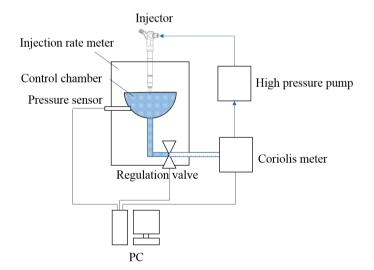


Figure 3.5: Schematic depiction of an injection rate meter.

Parameters	Units	Values
Fuel type		n-heptane
Fuel temperature	Κ	293
Fuel pressure	bar	200, 400, 600, 800, 1000, 1200, 1500
Control chamber temperature	Κ	323
Control chamber pressure	bar	25
Injection frequency	Hz	20
Number of shots	shot	200
Measuring range	mg/shot	0.4 - 150
Resolution	mg	0.01
Accuracy	mg/shot	$\pm 0.05~({\rm range}~0$ - 50 mg/shot)
	mg/shot	$\pm~0.2~(\mathrm{range}~0$ - 150 mg/shot)

Table 3.2: Experimental conditions for injection rate measurement.

# 3.4 Spray Imaging

A high-speed video camera was used to capture shadowgraph images of liquid sprays in a constant volume chamber using an LED light and a diffuser. Figure 3.6 shows a schematic depiction of the experimental setup. The images were post-processed and analyzed to determine spray characteristics such as the spray tip penetration and spray plume angles. The experimental conditions (including the high speed video camera settings for the spray imaging experiments) are listed in Table 3.3. Back illumination is a robust method for measuring penetration and spray plume angles because it creates a clear boundary between the liquid spray region and the surrounding air, giving a high signal to noise ratio.

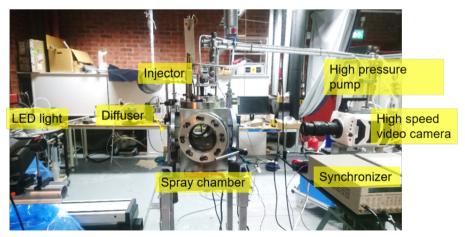


Figure 3.6: Setup of spray imaging test.

Parameters	Units	Values
Injector		Divergent 6 hole, Convergent 6 hole, Divergent 10 hole, Straight 10 hole
Fuel type		n-heptane
Fuel temperature	Κ	293
Fuel pressure	bar	200, 400, 600, 800, 1000, 1200, 1500
Injection mass	$\mathrm{mg}$	27
Chamber gas		air
Chamber gas pressure	bar	1, 6
Chamber gas temperature	Κ	293
Frame rate	$_{\rm fps}$	19000
Image size	pixel $\times$ pixel	$768 \times 768$
Image resolution	$\mathrm{mm/pixel}$	0.1489

Table 3.3: Experimental conditions for spray imaging.

## 3.5 Phase Doppler Interferometry

An Artium 2D Phase Doppler Interferometer (PDI) was used for droplet size measurement. The PDI system consists of a transmitter, receiver, and analyzer as shown in Figure 3.7. The two laser beams emitted by the transmitter intersect to create a measurement volume. The interferometer was used in refractive mode to maximize signal strength and quality, and a receiver was positioned with an off-axis angle of 34 degrees. The PDI settings and conditions used in these experiments are listed in Table 3.4. A programmable three-axis traverse system was used to control the measurement position. The measurement position used in this work was 80 mm downstream of the injector tip and 5 mm outside the spray core. This position was chosen because the droplet number density at the center of the spray was too high to permit the gathering of reliable droplet data. The divergent 6-hole injector was used in the PDI experiments because the droplet number density in the regions just outside the center of its spray plumes was low enough to enable reliable measurement. Even so, at the studied high injection pressures, the droplet number density became high when the injection rate was high, greatly reducing the number of validated droplets. The measurement time window was chosen such that droplet size was only measured during the injection event. Results for a typical time window together with the corresponding pulse input and injection rate trace are shown in Figure 3.8. There is a small delay between the needle opening signal and the start of size measurement because of the delayed appearance of the liquid spray. Similarly, at the end of the measurement period, there is a delay between the closing of the needle and the end of spray ejection. The measurement time window was chosen to end when the droplet velocity fell to two-thirds of its initial value (see Figure 3.8).

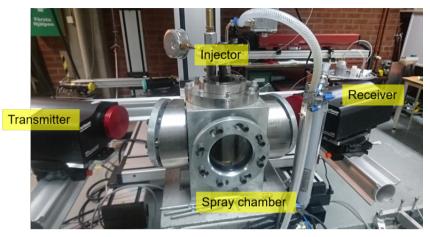


Figure 3.7: The PDI measurement apparatus.

Table 3.4:	Measurement	conditions	for	Phase	Doppler	Interferometry.
<b>T</b> able 0.1.	mousuiomon	conditions	TOT	I HODO	Doppier	inter on one y.

Parameters	Units	Values
Injector		Divergent 6 hole
Fuel type		n-heptane
Fuel temperature	Κ	293
Fuel pressure	bar	200, 400, 600, 800, 1000, 1200, 1500
Chamber gas		air
Chamber gas temperature	Κ	293
Chamber gas pressure	bar	1
Energizing time	$\mathbf{ms}$	3
Wavelength of lasers	nm	532, 561
Focal length of transmitter	$\mathbf{m}\mathbf{m}$	350
Beam diameter	$\mathbf{m}\mathbf{m}$	2.33
Expander factor		1.00
Frequency shift	MHz	40
Collection angle	degree	34
Static range	$\mu { m m}$	0.6 - 93.7
Index of refraction		1.45
Measured number of droplets		> 10000
Measuring range	$\mu { m m}$	0.6 - 93.7
Size accuracy	$\mu { m m}$	$\pm 0.5$
Size resolution	$\mu { m m}$	$\pm 0.5$

## 3.6 Particle Image Velocimetry

Particle Image Velocimetry (PIV) was used in this study to investigate spray-induced air motion; the experimental setup used for this purpose is shown in Figure 3.9. PIV is an

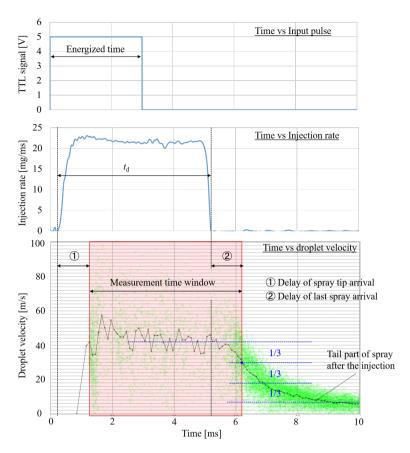


Figure 3.8: Measurement time window for PDI experiments.

optical two dimensional flow-field velocity measurement technique, and was performed using a system consisting of a double-pulse Nd-YAG laser, CCD camera, synchronizer, PC, and particle seeder. The laser's second harmonic (532 nm) was used to illuminate regions of the flow field containing seeded particles, and a laser sheet ( $\approx 1 \text{ mm thick}$ ) was formed using lenses. The relationship between the laser sheet's properties and the capture range is shown in Figure 3.10. The laser sheet passed through the center of a spray plume, and air motion images were captured from the side of the constant volume chamber. The image resolution of the CCD camera was  $2660 \times 1776$  pixels. The synchronizer controlled the activation timing of the laser and camera relative to the injection. The delay between the activation of the 1st and 2nd lasers was set to 200  $\mu$ s based on the velocity of the target flow and the results of preliminary tests. Spray images were captured at different time points after the start of injection by changing the timing of the injection pulse; 30 images were captured at each timing and averaged. A Laskin-type aerosol generator was used to inject small particles of olive oil into the constant volume chamber through the air intake pipe. It is important when seeding particles to ensure that their size is

appropriate for the task at hand because the ability to track seeded particles is central to PIV measurement. The seeder generated small particles, mostly with diameters around  $1\mu m$ . Particles of this size are suitable for tracking turbulent or high speed gas flows [33]. The density of the seeded particles in the surrounding air is considerably lower than the density of the liquid droplets in the spray, so the optical signals from the seeded particles in the surrounding air were significantly weaker than those from the spray. Therefore, a physical mask was placed between the constant volume chamber and the camera to block intense scattered light from the spray. Despite this, there was still a strong signal from the spray that made it impossible to detect signals from seeded particles in the area close to the spray. Therefore, the investigation focused on the air flow vectors in a region some distance from the spray edge. Interrogation areas were defined to determine the displacement of the particles in the captured images, using grids small enough that one could reasonably assume the flow to be uniform within them. Recursive analysis was used to increase the accuracy of the measured velocities. Velocity calculations were first performed for a relatively large interrogation area  $(128 \times 128 \text{ pixels})$  and then for a smaller one  $(64 \times 64 \text{ pixels})$ . The experimental conditions for PIV measurement are listed in Table 3.5.

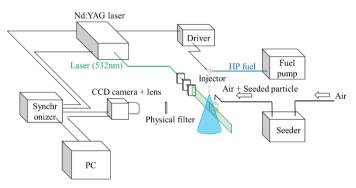


Figure 3.9: Schematic depiction of the PIV setup.

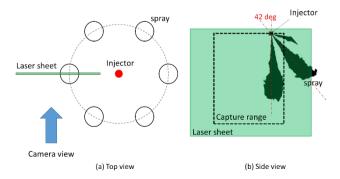


Figure 3.10: Schematic image of the spray imaging setup, (a) top view, (b) side view.

Parameters	Units	Values
Injector		Divergent 6 hole
		Convergent 6 hole
Fuel type		n-heptane
Fuel temperature	Κ	293
Fuel pressure	bar	200,600,1000,1500
Chamber gas		air
Chamber gas temperature	Κ	293
Chamber gas pressure	bar	1
Seeded particle		Olive oil
Seeded particle size	$\mu { m m}$	1
Camera resolution	$pixel^2$	$2352 \times 1768$
Image resolution	$\mathrm{mm/pixel}$	0.0435
Time delay of two lasers	$\mu { m s}$	200

Table 3.5: Measurement conditions for PIV measurement.

## 4 Methodology

#### 4.1 Spray image

Spray images taken with the high speed video camera were post-processed to determine the spray tip penetration length and breakup length. Captured spray images were binarized using a predefined threshold value; because the signal to noise ratio was high, the calculated spray tip penetration was relatively insensitive to the exact choice of threshold. A single spray plume was selected to calculate penetration, which was done by applying a mask. Spray tip penetration along the injector axis was determined by measuring the distance between the nozzle tip and the spray tip. However, this distance is the penetration along the injector axis, and therefore had to be rescaled to determine the penetration along the spray axis. This was done based on the camera's viewing angle and the spray direction (see Figure 4.1). An average of 20 images was used to estimate the penetration. Breakup points were determined from time-resolved spray tip penetration curves using the procedure developed by Hiroyasu and Arai [34]. A typical penetration curve is shown in Figure 4.2. The curve is plotted with a logarithmic scale, and the gradient at early timings clearly differs from that at later timings. Two lines extending these two gradients are superimposed on the plot; their point of intersection is defined as the breakup point. The breakup point is used to determine the breakup time and breakup length of the spray. If there is no clear change in gradient, the spray exhibits no detectable deceleration and the breakup point cannot be determined.

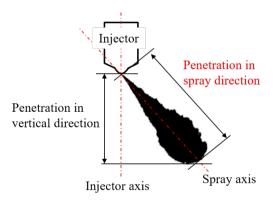


Figure 4.1: Penetration along the injector axis and the spray axis.

#### 4.2 Droplet size

Phase Doppler Interferometry systems are used to determine the sizes and velocities of multiple droplets simultaneously. The diameter of the particles is determined using a phase

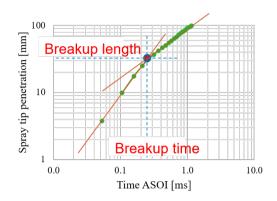


Figure 4.2: Identification of the breakup point based on a penetration curve [34].

Doppler interferometer, and particle velocity is determined using laser Doppler velocimetry. In the measurement volume, there is fringe pattern created by the intersection of two laser beams. A particle crossing the probe area magnifies this fringe pattern, creating a phase difference that is proportionate to the particle's size and which can be detected at the receiver. Smaller droplets have larger curvatures, which causes large divergence like a lens, leading to a small phase difference. Conversely, large droplets have low curvature, causing low divergence and a large phase difference. The receiver detects the phase difference, and droplet diameter is determined using an FFT method implemented in software. The measured signals are subjected to validation filters including phase validation and diameter validation to ensure the accuracy of the collected droplet data. Three statistical measures of droplet size are commonly used in spray analysis: the mean diameter  $(D_{10})$ , Sauter mean diameter  $(D_{32})$ , and 90% of accumulated volume fraction  $(Dv_{90})$ .  $D_{10}$  is a measure of the average size of all counted droplets; it therefore tends to reflect the size of the most numerous droplets. Consequently, it does not always accurately indicate the abundance of rarer large droplets.  $D_{32}$  is a measure of average droplet size based on droplet volume. Consequently, the  $D_{32}$  value for a sample containing a single large droplet and many small ones will differ markedly from that for a sample containing only small droplets. This variable is commonly used to compare spray characteristics because it can be considered more representative of the overall droplet size distribution than the mean diameter.  $Dv_{90}$ is the diameter for an accumulated volume fraction of 90% (see Figure 4.3). It can thus be considered a measure of the size of the largest droplets in the spray. Consequently, if  $Dv_{90}$  is  $20\mu m$ , the spray will contain almost no droplets with diameters above  $20\mu m$ . Measures of droplet size considered in this work include  $D_{10}$ ,  $D_{32}$ , and  $Dv_{90}$  at different injection pressures, the volume fraction distribution, and time-resolved D32 traces.

$$D_{10} = \frac{\sum N_i D_i}{\sum N_i} \tag{4.1}$$

$$Dv_{90} = \frac{\sum N_i D_i^3}{\sum N_i D_i^2}$$
(4.2)

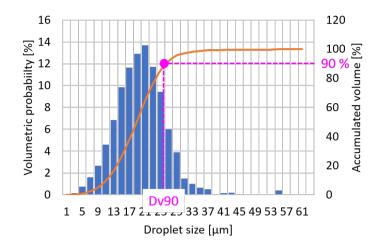


Figure 4.3: Volumetric probability and definition of Dv90.

#### 4.3 Large-scale air motion

Spray-induced air motion was evaluated using the PIV method. The output of this method is essentially a vector field in an interrogation area that can be analyzed to calculate air entrainment and the entrained air mass. Air entrainment is the air flow entrained into the spray, which helps drive atomization and mixture formation. In this work, a control line was defined along which air entrainment was calculated. Figure 4.4 shows this control line, which is 40 mm long and positioned 20 mm from the injector axis. This location was selected after a parameter study on the effects of varying the line location and length; the chosen length and location were found to be optimal for capturing trends and differences in air motion at different injection pressures and injection masses. The vectors closest to the control line were selected and their components orthogonal to the line were calculated using Equation 4.3. Air entrainment was computed by averaging the orthogonal components at different time steps (Equation 4.4), and the air entrainment at each time step was integrated to obtain the total mass of entrained air moving through the control line (Equation 4.5)

$$u_{\perp} = \pm \frac{b(av - bu)}{a^2 + b^2}, v_{\perp} = \pm \frac{a(av - bu)}{a^2 + b^2}$$
(4.3)

Here, the air flow vector is  $\vec{U} = (u, v)$ , the component of the air flow vector orthogonal to the control line is  $\vec{U_{\perp}} = (u_{\perp}, v_{\perp})$ , and the control line vector is  $\vec{l} = (a, b)$ 

$$Q_{entrainment} = \overline{\sum \rho |\vec{U_{\perp}}|} \tag{4.4}$$

$$m_{entrained} = \int \sum \rho |\vec{U_{\perp}}| \, \mathrm{d}t \tag{4.5}$$

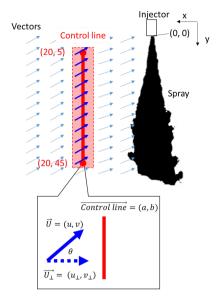


Figure 4.4: Line for air entrainment calculation

After calculating the air entrainment rate and the entrained mass, the ratio of the entrained mass and the injection mass was calculated. This ratio is a measure of the amount of air entrained per unit injection mass, and is calculated using equation (4.6).

$$\eta_{entrainment} = \frac{m_{entrained,max}}{m_{inj}} \tag{4.6}$$

# 5 Summary of Results

This section briefly outlines the main results of the research presented in this thesis; full details can be found in the appended papers.

### 5.1 The effect of ultrahigh injection pressures

A major focus of the work presented here was on the effects of elevated injection pressures on spray properties and particulate emissions. The main results obtained in this area are summarized below.

1. As the injection pressure increased, the injection event was shortened due to the high flow rates caused by the high fuel pressure, as shown in Figure 5.1; at the highest tested injection pressures, the injection duration was half that needed at an injection pressure of 200 bar. Shortening the injection event in this way enables a wider range of injection strategies to be used.

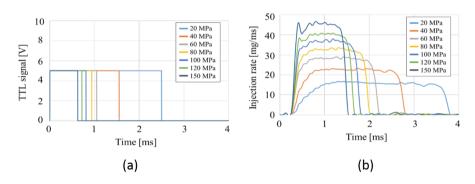


Figure 5.1: Injection rates at different injection pressures. (a):input pulse, (b): injection rate)

- 2. Higher injection pressures resulted in more rapid spray development, as demonstrated by the time-resolved spray tip penetration traces presented in Figure 5.2. This increased the rate at which the spray was distributed in space within the cylinder. However, it could also cause significant wall wetting if the start of injection timing is not optimized. The spray tip penetrations at the end of injection (EOI) timing were similar (see pink dots in Figure 5.2) for all of the tested injection pressures, but higher injection pressures yielded longer sprays after EOI.
- 3. Atomization improved at higher injection pressures, as clearly shown in Figure 5.3 (a). There were substantial reductions in the Sauter Mean Diameter (SMD) and Dv90, but the mean diameter (Dv10) did not change significantly. Figure 5.3(b) shows the abundance of large droplets in the sprays at different injection pressures; as can be seen, there were almost no no droplets larger than  $20\mu$ m when the injection

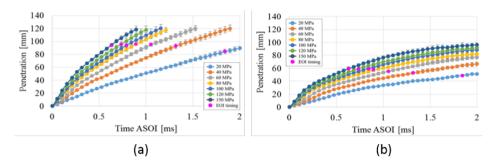


Figure 5.2: Spray tip penetrations at different injection pressures with a constant injection mass of 27 mg. (a) 1 bar backpressure, (b) 6 bar backpressure.

pressure was above 600 bar. This improvement in atomization should enhance evaporation and improve mixture formation in the cylinder. Interestingly, droplet size decreased markedly between injection pressures of 200 bar and 800 bar, but less so between 1000 bar and 1500 bar.

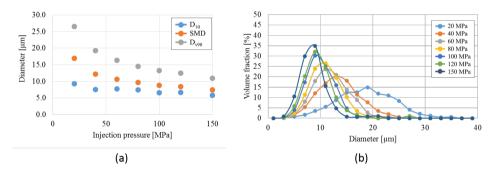
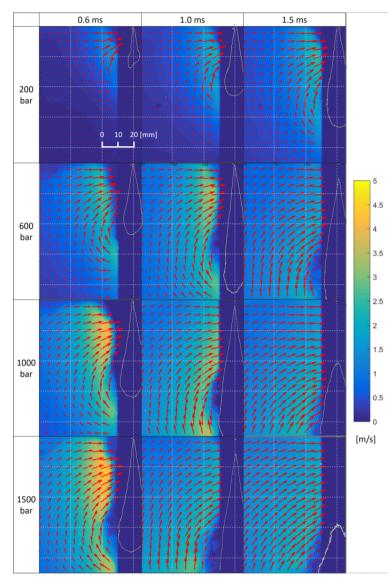


Figure 5.3: (a) Droplet sizes at different injection pressures, (b) Size distribution based on volume fraction.

4. Sprays formed at high injection pressures induced more large-scale air motion than those formed at low injection pressures because of their greater velocity, as shown in Figure 5.4. The spray-induced air motion is due to momentum exchange between spray droplets and the surrounding air. Sprays formed at higher pressures have a greater proportion of smaller droplets because they undergo more extensive atomization. High injection pressures therefore enhance the spray's interactions with the air. For injection pressures up to 1000 bar, air entrainment into the spray also increased with the injection pressure (see Figure 5.5 (a), which was beneficial for both atomization and mixture formation. However, the increase was much less pronounced for injection pressures above 1000 bar. This indicates that high injection pressures make it possible to rapidly induce substantial air motion, but that air entrainment also depends on the injection duration and is reduced when



the duration becomes very short, as occurs when the injection pressure is very high.

Figure 5.4: Vector fields at different injection pressures with a fixed injection mass of 27 mg.

5. Figure 5.5 (b) shows the ratio of the entrained mass to the injected mass. This ratio is a measure of the efficiency with which the injection and spray induce air motion. The ratio increases with the injection pressure, especially when the injection mass is small, indicating that injections with higher fuel pressures and small injection

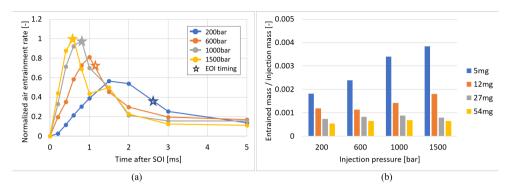


Figure 5.5: (a) Normalized air entrainment rates at different injection pressure with a fixed injection mass of 27 mg, (b) ratio of the entrained air mass to the injection mass for all combinations of injection mass and pressure.

masses induce air motion more efficiently than those with lower pressures or larger fuel masses. It may therefore be beneficial to perform multiple small injections when using high injection pressure systems in real engines. Such a multiple injection strategy could also help prevent piston/liner wetting because it would reduce the spray's penetration length.

#### 5.2 The effect of the nozzle type

- 1. Nozzle shape also influences the behavior and shape of the spray, as shown in Figure 5.6. Compared to the divergent nozzle, the convergent nozzle produced narrower, longer, and faster developing sprays. Accordingly, the convergent nozzle increased spray tip penetration, as demonstrated by comparing Figure 5.7 and Figure 5.2. This effect could be due to differences in the internal nozzle flow: convergent holes are likely to straighten the flow inside the nozzle hole. Increased spray tip penetration will increase the likelihood of piston/liner wetting, which is a major source of particulate emissions.
- 2. The induction of large scale air motion also depended significantly on the nozzle type. The spray from the divergent nozzle created more and stronger air motion over a greater volume (see Figure 5.4) than that from the convergent nozzle (see Figure 5.8). This was mainly because the two nozzles produced sprays with different shapes; wider sprays promote interaction between liquid droplets and the surrounding air. The air entrainment results presented in Figure 5.9(a) show that with a fixed injection mass, the spray from the divergent nozzle generated the same level of air entrainment at an injection pressure of 200 bar as the spray from the convergent nozzle thus induced air entrainment more efficiently than those from the convergent nozzle.
- 3. The ratio of entrained mass to injected mass for the convergent nozzle is shown

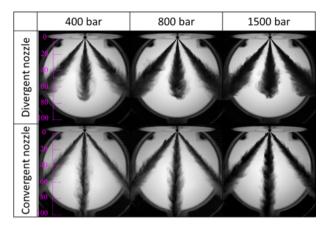


Figure 5.6: Spray images at EOI timing with a 27 mg injection mass.

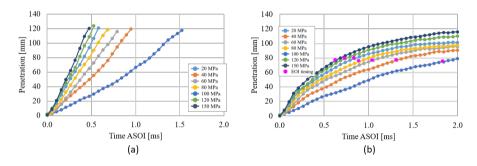


Figure 5.7: Spray tip penetrations at different injection pressures with a 27 mg injection mass, (a) 1 bar back pressure, (b) 6 bar back pressure.

in Figure 5.9(b). The ratios are lower than those for the divergent nozzle, but the trend is similar: air motion is most efficiently induced by a combination of a high injection pressure and a low injection mass. The use of low injection masses may be particularly beneficial for convergent nozzle injectors because the sprays formed with large injection masses exhibited high penetration soon after injection, and would thus have a high likelihood of causing wall wetting.

4. The usefulness of convergent nozzles is likely to be limited because of the spray shape that they produce. Sprays formed with high injection masses are not optimal because they are likely to have high penetration lengths, leading to high particulate emissions. This problem could potentially be avoided by performing multiple small injections or injecting into a high backpressure. Divergent nozzles appear to be more generally applicable because the sprays from such nozzles have relatively short penetration lengths, although there is a possibility that the spray plumes may coalesce if the back pressure is too high or under flash boiling conditions.

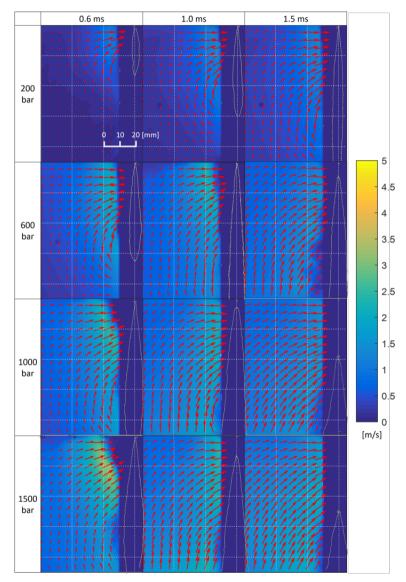


Figure 5.8: Vector fields generated at different injection pressures with a fixed injection mass of 27 mg using the convergent nozzle.

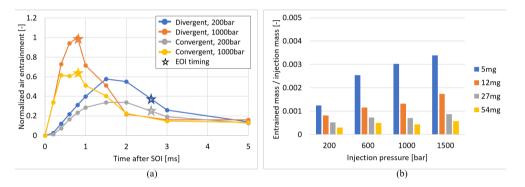


Figure 5.9: (a) Normalized air entrainment rates for different nozzle types, (b) ratio of the entrained air mass to the injection mass for the convergent nozzle.

# 6 Future work

The main objective of this project is to clarify the potential of high pressure fuel injection systems for GDI engines and the challenges associated with their use. The project focuses on three main issues: spray characteristics, mixture formation, and combustion characteristics. The spray investigations presented in this thesis together with preliminary engine test results and studies on mixture formation have revealed the major benefits of high injection pressures, namely better atomization and more air entrainment.

### 6.1 Studies on mixture formation in an optical engine

Because mixture formation strongly affects combustion quality and emissions, studies on mixture formation and homogeneity will be needed to understand why higher injection pressures reduce PN emissions. Planar Laser-Induced Fluorescence (pLIF) will therefore be used to investigate the effect of high injection pressures on the fuel vapor distribution.

### 6.2 Single-cylinder engine tests with an improved injector

An optimized injector will be identified based on the results of the spray investigations and preliminary single-cylinder engine tests. This will be necessary because the injectors used in the first parts of this project are more suitable for spray investigations than for a practical GDI engine. It is expected that the use of the optimized injector will both improve mixture formation and reduce particulate emissions.

## References

- [1] IEA, "Iea world energy balances 2019." https://webstore.iea.org/world-energy-balances-2019.
- [2] EEA, "Final energy consumption by sector and fuel in europe." https://www.eea.europa.eu/data-and-maps/indicators/final-energy-consumptionby-sector-10/assessment.
- [3] Delphi Technologies, "Worldwide emissions standards: Passenger cars and light duty vehicles 2020/21." https://www.delphi.com/innovations/emissions-standardsbooklets.
- [4] ICCT, "CO2 emission standards for passenger cars and light-commercial vehicles in the European Union." https://theicct.org/publications/ldv-co2-stds-eu-2030-updatejan2019.
- "BCG [5] Green Car Congress, forecasts electrified vehiclesto take half of global auto market by 2030;hybrids to dominate." https://www.greencarcongress.com/2017/11/20171103-bcg.html.
- [6] G. Saliba, R. Saleh, Y. Zhao, A. A. Presto, A. T. Lambe, B. Frodin, S. Sardar, hector Maldonado, C. Maddox, A. A. May, G. T. Drozd, A. H. Goldstein, L. M. Russell, F. Hagen, and A. L. Robinson, "Comparison of Gasoline Direct-Injection (GDI) and Port Fuel Injection (PFI) Vehicle Emissions: Emission Certification Standards, Cold-Start, Secondary Organic Aerosol Formation Potential, and Potential Climate Impacts," *Environmental Science and Technology*, vol. 51, pp. 6542–6552, 2017.
- [7] W. F. Piock, B. Befrui, A. Berndorfer, and G. Hoffmann, "Fuel Pressure and Charge Motion Effects on GDi Engine Particulate Emissions," *SAE International Journal of Engines*, vol. 8, pp. 464–473, 2015.
- [8] Delphi Technologies, "350-Bar GDi System." https://www.delphi.com/featuredtechnologies/350-bar-gdi-system.
- [9] T. Pauer, H. Yilmaz, J. Zumbrägel, and E. Schünemann, "New Generation Bosch Gasoline Direct-injection Systems," *MTZ worldwide*, vol. 78, pp. 16–23, 2017.
- [10] S. Buri, H. Kubach, and U. Spicher, "Effects of increased injection pressures of up to 1000 bar - Opportunities in stratified operation in a direct-injection spark-ignition engine," *International Journal of Engine Research*, vol. 11, pp. 473–484, 2010.
- [11] Z. Lee and S. Park, "Particulate and gaseous emissions from a direct-injection spark ignition engine fueled with bioethanol and gasoline blends at ultra-high injection pressure," *Renewable Energy*, vol. 149, pp. 80–90, 2020.
- [12] T. Kaminaga, K. Yamaguchi, S. Ratnak, J. Kusaka, T. Youso, T. Fujikawa, and M. Yamakawa, "A Study of Combustion Characteristics of a High Compression Ratio SI Engine with High Pressure Gasoline Injection," *SAE Technical Paper*, 2019.
- [13] M. Medina, M. Fatouraie, and M. Wooldridge, "High-Speed Imaging Studies of Gasoline Fuel Sprays at Fuel Injection Pressures from 300 to 1500 bar," SAE Technical Paper, 2018.

- [14] M. Migliaccio, A. Montanaro, C. Beatrice, P. Napolitano, L. Allocca, and V. Fraioli, "Experimental and numerical analysis of a high-pressure outwardly opening hollow cone spray injector for automotive engines," *Fuel*, vol. 196, pp. 508–519, 2017.
- [15] A. Montanaro, L. Allocca, and G. Meccariello, "Effects of Ultra-High Injection Pressures up to 100 MPa on Gasoline Spray Morphology," SAE Technical Paper, 2020.
- [16] R. Payri, A. Garcia, V. Domenech, R. Durrett, and A. P. Torres, "Hydraulic Behavior and Spray Characteristics of a Common Rail Diesel Injection System Using Gasoline Fuel," SAE Technical Paper, 2012.
- [17] J. Peer, F. Backes, H. Sauerland, M. Härtl, and G. Wachtmeister, "Development of a High Turbulence, Low Particle Number, High Injection Pressure Gasoline Direct Injection Combustion System," *SAE International Journal of Engines*, vol. 9, pp. 2301–2311, 2016.
- [18] L. Postrioti, A. Cavicchi, G. Brizi, F. Berni, and S. Fontanesi, "Experimental and Numerical Analysis of Spray Evolution, Hydraulics and Atomization for a 60 MPa Injection Pressure GDI System," SAE Technical Paper, 2018.
- [19] V. Rossi, N. Silvestri, and M. Medda, "Experimental Investigations on Engine-Out Emissions Sensitivity to Fuel Injection Pressure of a High-Performance DISI Single Cylinder Engine," SAE Technical Paper, 2019.
- [20] J. Song, Z. Lee, J. Song, and S. Park, "Effects of injection strategy and coolant temperature on hydrocarbon and particulate emissions from a gasoline direct injection engine with high pressure injection up to 50MPa," *Energy*, vol. 164, pp. 512–522, 2018.
- [21] A. Stadler, R. Brunner, G. Wachtmeister, and H. Sauerland, "Experimental Investigations on High Pressure Gasoline Injection up to 800 bar for Different Combustion Modes," *MTZ worldwide*, vol. 80, pp. 52–57, 2019.
- [22] W. Imoehl, L. Gestri, M. Maragliulo, L. Del-Frate, M. Klepatsch, and R. Wildeson, "A DOE Approach to Engine Deposit Testing used to Optimize the Design of a Gasoline Direct Injector Seat and Orifice," SAE International Journal of Fuels and Lubricants, vol. 5, pp. 1078–1095, 2012.
- [23] J. Wetzel, "Optical analysis of the influence of injector hole geometry on mixture formation in gasoline direct injection engines," Automotive and Engine Technology, vol. 1, pp. 57–67, 2016.
- [24] M. Wirth, D. Zimmermann, J. Caine, A. Schamel, A. Storch, K. Ries-Mueller, K.-P. Gansert, G. Pilgram, R. Ortmann, and G. wuerfel, "The Next Generation of Gasoline Direct Injection: Improved Fuel Economy and Optimizaed System Cost," Advanced engine design performance, pp. 139–152, 2003.
- [25] J. Sim, J. A. Badra, and H. G. Im, "Hollow-Cone Spray Modeling for Opeing Piezoelectric Injector," 54th AIAA Aerospace Sciences Meeting, 2016.
- [26] C. Preussner, C. Döring, S. Fehler, and S. Kampmann, "GDI: Interaction Between Mixture Preparation, Combustion System and Injector Performance," SAE Technical Paper, 1998.
- [27] C. Baumgarten, Mixture Formation in Internal Combustion Engines. Reading, Massachusetts: Springer-Verlage Berlin Heidelberg, 2006.

- [28] A. H. Lefebvre, Atomization and Sprays. CRC Press, 1989.
- [29] W. V. Ohnesorge, "Die Bildung von Tropfen an Düsen und die Auflsung flüssiger Strahlen," ZAMM - Journal of Applied Mathematics and Mechanics, vol. 16, pp. 355– 358, 1936.
- [30] J. Stegeman, J. Seebode, J. Baltes, C. Baumgarten, and G. P. Merker, "Influence of throttle effects at the needle seat on the spray characteristics of a multihole injection nozzle," *ILASS-Europe*, 2002.
- [31] A. H. Lefebvre and V. G. McDonell, Atomization and Sprays, Second Edition. CRC Press, 2017.
- [32] DENSO CORPORATION, "MAZDA SKYACTIV-D Engine (EURO 6), Common Rail System (CRS) Service Manual."
- [33] A. Melling, "Trace particles and seeding for particule image velocimetry," Measurement Science and Technology, vol. 8, pp. 1406–1416, 1997.
- [34] H. Hiroyasu and M. Arai, "Structures of Fuel Sprays in Diesel Engines," SAE Transactions, vol. 99, pp. 1050–1061, 1990.

# Part I Appended Papers A–B

# Appended Publications A–B